remote sensing

MDPI

Article

Assessment and Prediction of Sea Level and Coastal Wetland Changes in Small Islands Using Remote Sensing and Artificial Intelligence

Nawin Raj * and Sarah Pasfield-Neofitou

School of Mathematics, Physics and Computing, Springfield Campus, University of Southern Queensland, Springfield, QLD 4300, Australia; u1150054@umail.usq.edu.au
* Correspondence: nawin.raj@usq.edu.au

Abstract: Pacific Island countries are vulnerable to the impacts of climate change, which include the risks of increased ocean temperatures, sea level rise and coastal wetland loss. The destruction of wetlands leads not only to a loss of carbon sequestration but also triggers the release of already sequestered carbon, in turn exacerbating global warming. These climate change effects are interrelated, and small island nations continuously need to develop adaptive and mitigative strategies to deal with them. However, accurate and reliable research is needed to know the extent of the climate change effects with future predictions. Hence, this study develops a new hybrid Convolutional Neural Network (CNN) Multi-Layer Bidirectional Long Short-Term Memory (BiLSTM) deep learning model with Multivariate Variational Mode Decomposition (MVMD) to predict the sea level for study sites in the Solomon Islands and Federated States of Micronesia (FSM). Three other artificial intelligence (AI) models (Random Forest (FR), multilinear regression (MLR) and multi-layer perceptron (MLP) are used to benchmark the CNN-BiLSTM model. In addition to this, remotely sensed satellite Landsat imagery data are also used to assess and predict coastal wetland changes using a Random Forest (RF) classification model in the two small Pacific Island states. The CNN-BiLSTM model was found to provide the most accurate predictions (with a correlation coefficient of >0.99), and similarly a high level of accuracy (>0.98) was achieved using a Random Forest (RF) model to detect wetlands in both study sites. The mean sea levels were found to have risen 6.0 $\pm$ 2.1 mm/year in the Solomon Islands and 7.2 $\pm$ 2.2 mm/year in the FSM over the past two decades. Coastal wetlands in general were found to have decreased in total area for both study sites. The Solomon Islands recorded a greater decline in coastal wetland between 2009 and 2022.

Keywords: bidirectional long short-term memory (BiLSTM); convolutional neural network (CNN); deep learning (DL); machine learning (ML); mean sea level (MSL); multi-layer perceptron (MLP); multilinear regression (MLR); random forest (RF)

Citation: Raj, N.; Pasfield-Neofitou, S. Assessment and Prediction of Sea Level and Coastal Wetland Changes in Small Islands Using Remote Sensing and Artificial Intelligence. *Remote Sens.* **2024**, *16*, 551. https://doi.org/10.3390/rs16030551

Academic Editors: Peter M. Atkinson and Ce Zhang

Received: 1 December 2023
Revised: 4 January 2024
Accepted: 30 January 2024
Published: 31 January 2024

1. Introduction

Small island developing states (SIDS), including those in the Pacific, are disproportionally threatened by climate change [1]. Pacific Island countries and territories, including the Federated States of Micronesia (FSM) and the Solomon Islands, depicted in Figure 1, are often described as being on the "frontline", with increases in global average temperature predicted to not only increase the intensity and frequency of disaster events [2] but to lead to sea level rise. This, in turn, will exacerbate coastal erosion [3], impacting valuable ecosystems, including wetlands. Recent developments in both Earth observation methods, including the satellite and geodetic data obtained via remote sensing (RS), and artificial intelligence (AI) have increased opportunities for not only rapid, accurate assessment of sea level, coastlines and vegetation but also for researchers to make predictions about how they will change, allowing communities and policymakers to better respond to climate threats.

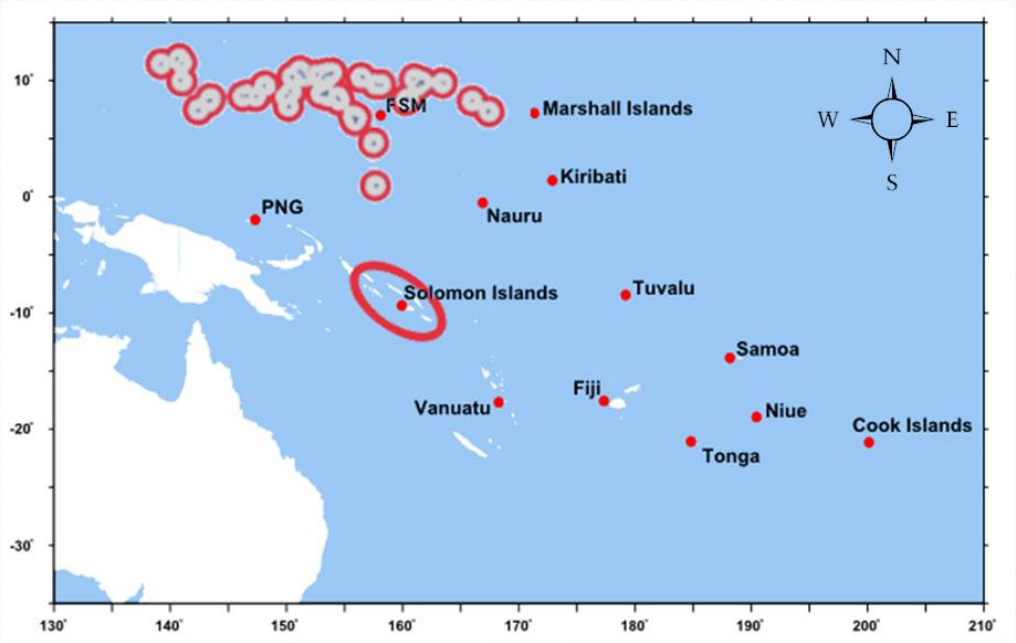

Figure 1. Study region. The red circles show the islands of the two countries under study. Source: Pacific Sea Level Monitoring Project (http://www.bom.gov.au/pacific/projects/pslm/index.shtml, accessed on 15 May 2023, modified to show details of FSM).

Globally, sea level rise (SLR) is caused by a combination of the thermal expansion of ocean waters and freshwater input from melting glaciers and ice sheets, increasing the total volume of water in the sea [4]. At a regional level, ocean currents, wind and pressure changes can contribute to SLR [5]. While international climate negotiations often focus on air temperature thresholds [6], even a 1.5 °C target is predicted to result in significant SLR.

Between 1901 and 1990, the global mean SLR was 1.35 mm/year, faster than any century in at least 3000 years [7]; between 1993 and 2018, this rate accelerated to 3.25 mm/year, and it is projected to rise further. Yet, SLR varies greatly based on geography. Church et al. [8] highlight the variability in sea levels between 1993 and 2001, with large rises across the western Pacific and eastern Indian Oceans and drops in the eastern Pacific and western Indian Oceans. In the western Pacific nations of Micronesia and the Solomon Islands, Klein [9] reports that SLR of up to 12 mm/year, more than triple the global average, has occurred since the early 1990s. As a result, small island nations are predicted to suffer wetland degradation, increased flooding and saltwater intrusion as a result of SLR [10]. Mangrove wetlands are known as both a "bioshield" protecting coastlines and reefs and one of the Pacific's most vital "blue carbon" sinks.

While some research has been undertaken in both the FSM and Solomon Islands, there has been relatively little scholarly attention paid to these islands in comparison with areas of Melanesia, such as Fiji [11]. The need for additional study is evident given the unclear relationships between complex climate variables and the conflicting accounts and predictions of ecosystem loss. Projections for the Solomon Islands' mangroves, for example, range from no change [12] to a loss of 68% [10]. Remote sensing technologies, including satellite and Tide Gauge (TG) observations, with the application of new AI approaches to predict sea levels in these areas, provide an important opportunity to accurately assess and predict the interlinked challenges facing not only Pacific Island nations but the entire world. In response to these needs, this study employs new data-driven hybrid AI model(s) to provide predictions of the sea level in the FSM and the Solomon Islands using geodetic data. Hence, a new hybrid CNN-BiLSTM deep learning model is developed with a Multivariate Variational Mode Decomposition (MVMD) technique for

the prediction of sea levels. Furthermore, it will utilise Landsat satellite imagery to detect coastal wetland changes in the FSM and the Solomon Islands.

Convolutional Neural Networks (CNNs) have been successfully combined with TG data to predict sea levels in other South Pacific islands [13], as well as worldwide sea level surges [14]. Bidirectional Long Short-Term Memory (BiLSTM) deep learning methods have also shown high levels of accuracy in predicting the sea level in Kiribati and Tuvalu [15] and wave height in Australia [16], with the BiLSTM model's wave predictions outperforming all other models, including BiLSTM, EEMD-SVR and SVR alone. Hybrid CNN-LSTM methods have been employed to predict phenomena as diverse as flooding [17] and air quality [18]. As Sharma et al. note, CNNs employ efficient multistage architecture via convolution, yet additional improvements can be achieved using a secondary LSTM-based deep learning architecture, the LSTM helping to vanish gradient issues and explore sequential data using unique gates. As a result, the amalgamation of CNNs with LSTM-based architecture is an active area of research.

2. Materials and Methods

The tide gauge (TG) and climate data were obtained from the BOM's Pacific Sea Level and Geodetic Monitoring (PSLGM) project (http://www.bom.gov.au/pacific/projects/pslm/index.shtml, accessed on 19 March 2023), as shown in Table 1.

Table 1. The geographical details of the study site locations in the Pacific Ocean.

State	Tide Gauge Location	Geographical Location
FSM	Pohnpei	6°50′59.99″N and 158°12′60.00″E
Solomon Islands (SI)	Honiara	9°25′59.99″S and 159°56′60.00″E

The PSLGM includes a network of geodetic monitoring stations implemented and maintained by Geoscience Australia, providing Global Navigation Satellite System (GNSS) measurements, which permit the absolute determination of the vertical height of the gauges measuring the sea level. In addition to sea level data (meters above TG zero), the PSLGM also provides measurements of climate variables, including water and air temperatures (in degrees Celsius), barometric pressure (in hPa), residual and adjusted residual sea levels (in meters), wind direction (in Degrees True), as well as wind gust and speed (in m/s).

The locations described in Table 1 were used to define areas of interest using National Aeronautics and Space Administration (NASA) Landsat mission (https://landsat.gsfc.nasa.gov/data/, accessed on 19 March 2023) and the Global Mangrove Watch (https://www.globalmangrovewatch.org/, accessed on accessed on 19 March 2023) satellite images.

2.1. Data Preprocessing, Partitioning and Normalisation

Missing or erroneous values in the PSLGM dataset are set to a value of −9999, which must either be removed or replaced via interpretation before analysis can take place. Any month with more than 1000 missing values (i.e., >15% of the total data points) was excluded from the analysis. Then, the remaining data were checked to ensure no more than a maximum of 72 missing consecutive hourly values (i.e., three days) in any given column. Finally, interpolation was conducted using the popular Pandas Linear method in Python.

Lags are an important aspect of time-series data modelling [19]. To determine significant lags, the Auto-Correlation Function (ACF) and Partial Auto-Correlation Function (PACF) were computed, which take into account seasonal and cyclic trends and residuals to find correlations [20]. Figure 2 shows the results of this analysis for the FSM.

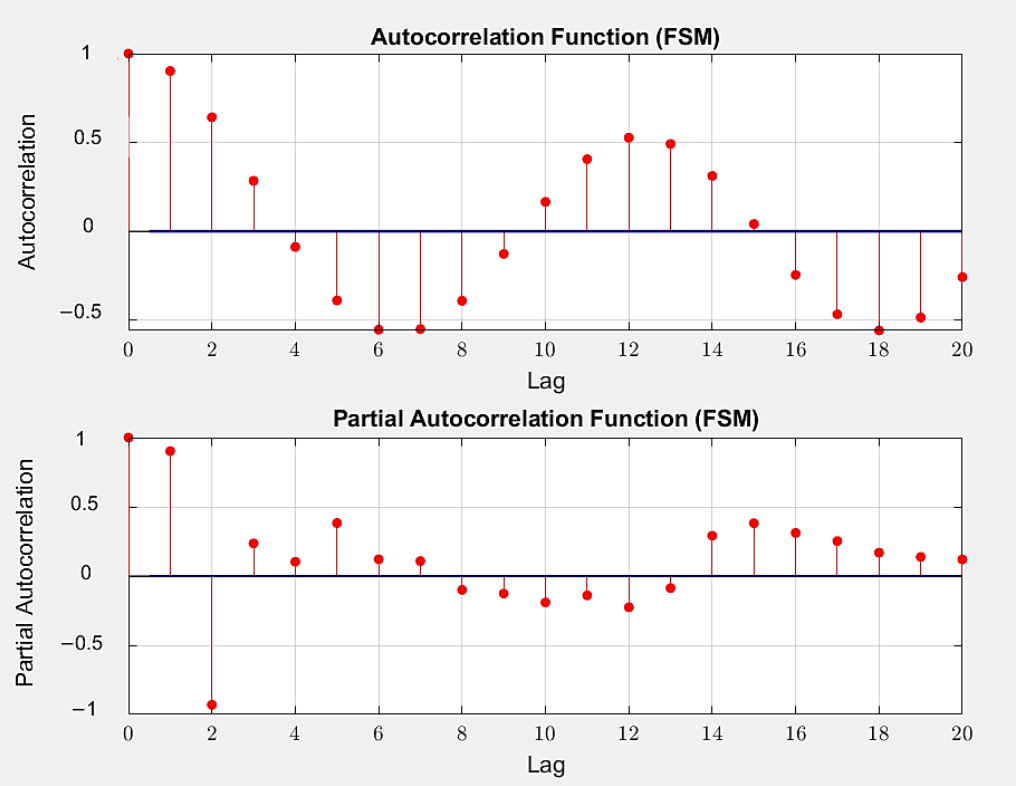

Figure 2. ACF and PACF of FSM sea level showing 20 lags at 95% confidence interval.

Signal decomposition is the extraction and separation of signal components into their intrinsic mode functions (IMFs) [21]. Multivariate Variational Mode Decomposition (MVMD) was used, which has the ability to simultaneously capture the non-stationary and non-linearity of a multichannel signal to overcome mode-mixing issues [22]. This procedure helps extract hidden features from the sea level time-series signal and facilitate effective AI model learning from these input variables for accuracy in forecasting. Figure 3 shows the sea level signal decomposition using MVMD for the FSM.

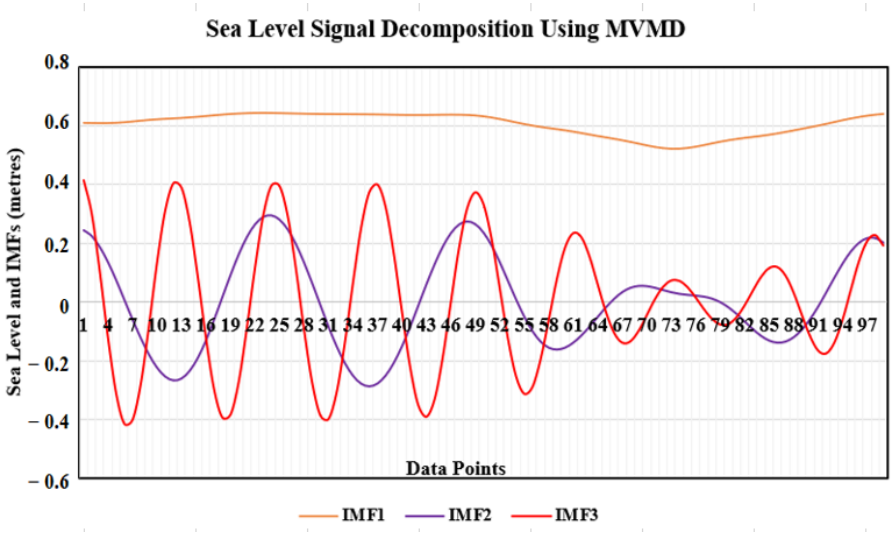

Figure 3. FSM sea level signal and decomposed IMFs of 40 data points.

The corrected oceanic dataset containing the input and target variables was then partitioned into training, validation and testing, as shown in Table 2.

Table 2. Oceanic data partition into training, validation and testing for modelling.

Partition	Training	Validation	Testing
SI Oceanic Dataset	September 1994–December 2011	December 2014–May 2017	June 2017–February 2023
FSM Oceanic Dataset	December 2001–October 2014	November 2014–June 2018	July 2018–February 2023

Periods for which data were missing are omitted from the partitions, as described above. Note that the TG record for the Solomon Islands location is longer (starting in 1994) than for the FSM facility, as the TG at this location was only installed in 2001.

Figure 4 shows the correlation of the Solomons Islands' sea level with its predictor inputs. Similar analysis was undertaken for the FSM.

	Water temp.	Air Temp.	Barometric Press.	Wind Direction	Wind Gust	Wind Speed	M1	M2	M3	t−1	t−2	t−3	Sea Level
Water Temp.	1	0.31	−0.39	0.051	−0.034	0.012	0.6	0.0048	0.013	0.32	0.32	0.32	0.32
Air Temp.	0.31	1	−0.19	−0.23	0.21	0.22	0.1	−0.024	−0.1	0.021	0.04	0.063	0.009
Barometric Press.	−0.39	−0.19	1	−0.15	−0.064	−0.056	−0.32	−0.0082	−0.18	−0.25	−0.27	−0.25	−0.22
Wind Direction	0.051	−0.23	−0.15	1	−0.15	−0.16	0.047	0.065	0.077	0.076	0.052	0.022	0.092
Wind Gust	−0.034	0.21	−0.064	−0.15	1	0.77	0.01	−0.05	0.0053	−0.0012	0.025	0.041	−0.031
Wind Speed	0.012	0.22	−0.056	−0.16	0.77	1	−0.00087	−0.039	−0.067	−0.011	0.023	0.049	−0.046
M1	0.6	0.1	−0.32	0.047	0.01	−0.00087	1	0.11	0.0009	0.59	0.59	0.57	0.6
M2	0.0048	−0.024	−0.0082	0.065	−0.05	−0.039	0.11	1	0.036	0.78	0.7	0.57	0.81
M3	0.013	−0.1	−0.18	0.077	0.0053	−0.067	0.00093	0.036	1	0.26	0.15	0.0044	0.29
t−1	0.32	0.021	−0.25	0.076	−0.0012	−0.011	0.59	0.78	0.26	1	0.96	0.86	0.96
t−2	0.32	0.04	−0.27	0.052	0.025	0.023	0.59	0.7	0.15	0.96	1	0.96	0.86
t−3	0.32	0.063	−0.25	0.022	0.041	0.049	0.57	0.57	0.0044	0.86	0.96	1	0.71
Sea Level	0.32	0.009	−0.22	0.092	−0.031	−0.046	0.6	0.81	0.29	0.96	0.86	0.71	1

Figure 4. Solomon Islands correlation matrix showing the correlation between the sea level and all predictor variables. The dark green areas show a strong correlation, yellow areas show weaker correlation and white cells show negative correlation. (t − 1), (t − 2), (t − 3)—are lags for 1, 2 and 3 years, respectively. M1, M2 amd M3 are IMF1, IM2 and IM3, respectively.

The final step of data preprocessing is normalisation using the equation:

$$x_{normalised\ data\ value} = \frac{x_{\text{actual data value}} - x_{\text{minimum of data values}}}{x_{\text{maximum of data values}} - x_{\text{minimum of data values}}} \quad (1)$$

This scaling process helps reduce the time taken in the learning stage of data modelling by avoiding the computation of large values [23]. Once modelling is complete, the values are converted back into their original form using the equation below:

$$x_{\text{actual data value}} = x_{normalised\ data\ values}(x_{\max} - x_{\min}) + x_{\min} \quad (2)$$

where x is the input data value, $x_{\min}$ is the overall minimum and $x_{\max}$ is the overall maximum value.

2.2. Sea Level Prediction

Machine Learning (ML), a subset of AI in which computer systems learn automatically with experience rather than being explicitly programmed, is commonly used in the analysis of ocean data, where traditional methods have many shortcomings [24]. Deep learning (DL) may be defined as a subset of ML and refers to techniques which layer algorithms

and computing units or "neurons" into artificial networks designed to mimic the brain. Researchers have predominantly used Artificial Neural Networks (ANNs), followed by Support Vector Machines (SVMs), to predict flooding and the use of mangroves for risk mitigation [25], particularly in conjunction with satellite data [26].

In the present study, four models were tested.

2.2.1. Multilinear Regression

Multiple linear regression or multilinear regression (MLR) can estimate the relationship between two or more explanatory variables and one response variable. An MLR model is a supervised learning algorithm which can be used, for example, to predict sea level given multiple input variables.

The formula for MLR is:

$$y = \beta_0 + \beta_1 X_1 + \beta_2 X_2 + \cdots + \beta_n X_n + \epsilon \quad (3)$$

where y is the predicted or expected value of the response or dependent variable, β_0 is the y-intercept (i.e., the value of y when all other parameters are set to 0), β_1 through β_n are the regression coefficients of the explanatory or independent variables X_1 through X_n (i.e., the effect that increasing the value of the independent variable has on the predicted y value) and ϵ is the model error (i.e., how much variation exists in the estimate of y).

2.2.2. Random Forest Model

A Random Forest (RF) model utilises a combination of tree predictors, where each tree depends on the values of a random vector sampled independently with the same distribution [27]. The algorithm applies the bootstrapping aggregation to tree-based learners [28]. These bootstrap samples of the training sets are selected repeatedly, and Gini impurity fits t_b trees in these samples. Then, the equation below is used to calculate the predicted values for unseen complexes:

$$y = \frac{1}{B} \sum_{b=1}^{B} t_b(x) \quad (4)$$

where B is the number of times the bootstrapping aggregation or "bagging" is performed, and x is the input variable.

2.2.3. Multi-Layer Perceptron

A Multi-Layer Perceptron (MLP) is a supervised ML algorithm [29], one of the simplest ANNs, in which the node's connections do not form a loop, i.e., the flow of information is unidirectional [30]. MLPs are some of the most widely used ML algorithms, capable of robust and efficient flood prediction [25]. While a single-layer perceptron consists of a single-layer output node directly connected to the input by a series of weights, a multi-layer perceptron is an interconnected network with multiple hidden layers [31]. In the hidden layers, the input data undergo a series of weighted sums, and after calculating the weighted summation of each hidden neuron, the result is applied to an activation function, f, and the result of this function is again weighted and summed to obtain the output [24]:

$$y_i = f\left(\sum_{j=1}^{n} x_j \cdot w_{ij} \right) \quad (5)$$

where x_j is the input vector from the previous layer, and w_{ij} is the weight vector, generating the scalar product $x_j \cdot w_{ij}$ [32].

2.2.4. Bidirectional Long Short-Term Memory

A Bidirectional Long Short-Term Memory (BiLSTM) model architecture consists of two long short-term memory (LSTM) networks. Long short-term memory (LSTM) neural networks are another type of ANN [30], which selectively memorise input [24].

LSTM networks comprise three layers: input, one or more hidden layer(s) and an output layer (similar to an MLP), with the neuron number in the input/output layer equivalent to the amount of feature space [33]. The memory cell(s) within the hidden layer have three gates: forget, input and output, and at every time step t, each gate is presented with the input x_t and the output of the memory cells at the previous time step, x_{t-1}.

At each time step, the cell state s_t and output h_t are calculated. The gates act as filters, with the forget gate deciding which particular is detached from the cell state, the input gate specifying which information supplements the cell state and the output gate deciding which data from the cell state are used as output [33]. Finally, the sigmoid function scales all values from 0 (forget completely) to 1 (remember completely):

$$f_1 = \text{sigmoid}\left(W_{f,x}X_t + W_{f,}X_{t-1} + b_f\right) \tag{6}$$

The second step is determined by the LSTM layer, which adds information to the network's cell states, by computing candidate values for s_t and activation values i_t :

$$s_t = \tanh(W_{s,x}\,x_t + W_{s,h}h_{t-1} + b_s)\,i_t = \text{sigmoid}(W_{i,x}\,x_t + W_{i,h}h_{t-1} + b_i) \tag{7}$$

The third step involves the design of new cell states s_t based on the results of the previous steps, with $\circ$ representing the Hadamard product:

$$s_t = f_t \circ s_{t-1} + i_t \circ S_t \tag{8}$$

The final step is the calculation of the output, h_t, using the following two equations:

$$O_t = \text{sigmoid}(W_{0,x}X_t + W_{0,h,}h_{t-1} + b_0)h_t = O_t \circ \tanh(s_t) \tag{9}$$

LSTM neural networks have a strong learning and predictive ability for time-series data such as sea surface temperature [24] and saltwater intrusion [34].

2.3. Model Evaluation

Following Raj [15], five statistical metrics were used to evaluate the performance of the models described above.

The first three equations are efficiency metrics, used to measure the accuracy of the models. The correlation coefficient r determines the relationship between two variables, indicating the strength of association, e.g., between the observed and predicted SLR. Willmott's Index of Agreement d indicates the ratio of the mean of square error and potential error, detecting proportional differences between the observed and predicted values. Legates and McCabe's Index LM is a more advanced index utilising the adjustment of comparisons in the evaluation of Willmott's Index.

1. Correlation coefficient (r)

$$r = \left[\frac{\sum_{i=1}^{n}(DO_i - MDO)(DS_i - MDS)}{\sum_{i=1}^{n}(DO_i - MDO)^2\sum_{i=1}^{n}(DS_i - MDS)^2}\right]^2$$

2. Willmott's Index of Agreement (d)

$$d = 1 - \left[\frac{\sum_{i=1}^{n}(DO_i - DS_i)^2}{\sum_{i=1}^{n}(\,|DS_i - MDO| + DO_i - MDS|)^2}\right]$$

3. Legates and McCabe's Index (*LM*)

$$LM = 1 - \left[\frac{\sum_{i=1}^{n}|(DS_i - DO_i)|}{\sum_{i=1}^{n}|DO_i - MDS|}\right], 0 \leq L \leq 1$$

The error metrics used for evaluation are the root mean square error (*RMSE*) and mean absolute error (*MAE*). The *RMSE* is the square root of the mean square error and measures the average difference in error between the predicted and observed values [35]. The *MAE* is the mean of the absolute errors between the predicted and observed values [36].

4. Root mean square error (*RMSE*)

$$RMSE = \sqrt{\frac{1}{n}\sum_{i=1}^{n}(DS_i - DO_i)^2}$$

5. Mean absolute error (*MAE*)

$$MAE = \frac{1}{n}\sum_{i=1}^{n}|(DS_i - DO_i)|$$

2.4. Wetland and Mangrove Detection

A Random Forest model using satellite data was also used for the detection of wetlands, with the Landsat data for supervised classification obtained from Surface Reflectance Tier 1 of the USGS Landsat 7 and 8 image classification dataset, at a 30 m digital elevation and with images selected based on the lowest prevalence of cloud cover.

Spectral indices were computed for the wetland mapping, including the Normalised Difference Mangrove Index (NDMI) [37], Modified Normalised Water Index (MNWI) [38], Simple Ratio Vegetation Index [39], Green Chlorophyll Vegetation Index (GCVI) [40] and normalised difference vegetation index (NDVI).

The NDVI is a simple graphical indicator of whether an area under observation contains live green vegetation [41]. It is often used as a proxy for vegetation productivity, and therefore overall health [42] and growth [43], and is calculated as follows:

$$NDVI = \frac{NIR - RED}{NIR + RED} \quad (10)$$

where NIR represents near-infrared and RED represents red wavelengths [44]. These bands contrast the absorption of chlorophyll pigment at the red end against the reflectance of mesophyll at the NIR end [41]. Healthy vegetation tends to absorb most of the light at the red end of the spectrum and reflect a large portion of the NIR light, while unhealthy or sparse vegetation will reflect more red light and less NIR light [45].

NDVI values can range between −1 and +1, with positive values representing vegetation of varying health and negative values representing other land use/land cover (LULC) classes [46]. A total of 330 samples were taken for the Solomon Islands and 340 for the FSM. These samples were then split into training (80%) and testing (20%) sets. The model used 200 trees and 5 randomly selected predictors per split. Each stratified point was checked with ground-based images, as shown in Figure 5, to evaluate the label for correct classification of the coastal wetland.

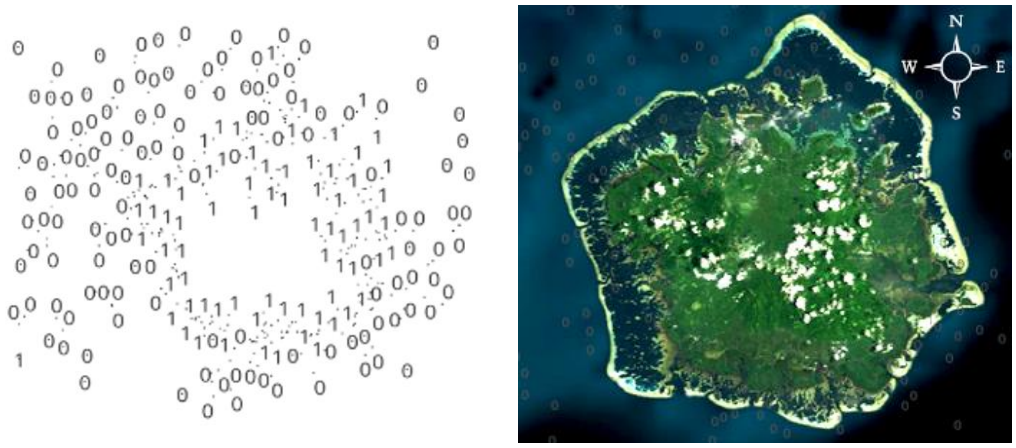

Figure 5. (**Left**): FSM stratified random points from classification with labels of 1 (coastal wetland) and 0 (non-coastal wetland). (**Right**): Google satellite image added below the points for calculation of accuracy.

Following evaluation, the class accuracy plugin in QGIS was used to compute the accuracy and the Kappa value for both study areas, using Equation (11) below. Figure 6 shows a close-up view of the stratified points:

$$K = \frac{Observed\ Agreement - Expected\ Agreement}{1 - Expected\ Agreement} \quad (11)$$

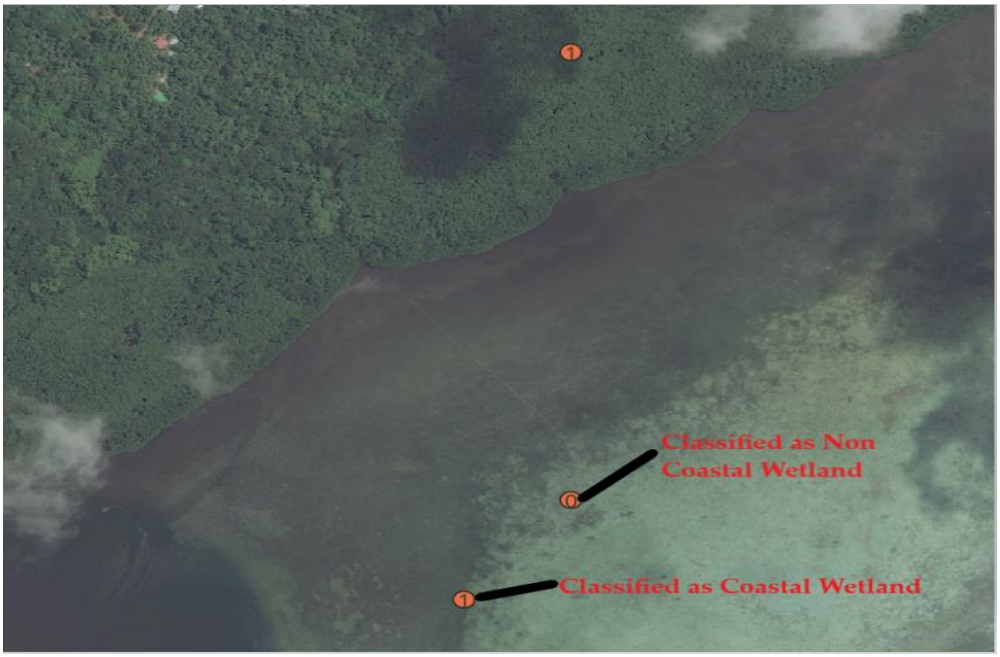

Figure 6. Stratified random points (for FSM) checked with ground-based Google satellite image. 0 denotes non-coastal wetland and 1 denotes coastal wetland.

3. Results

3.1. Model Performance Metrics for Sea Level Prediction Using Machine Learning

To examine how accurately the four models under investigation were able to predict the sea levels in both the Solomon Islands and FSM, as outlined in the first research question, this section presents the results relating to the efficiency and error metrics outlined in Section 2 above. Table 3 displays the model performance metrics for the Solomon Islands, with the CNN-BiLSTM model (in bold) achieving a superior performance across all metrics.

Higher values indicate a superior performance on the efficiency measures (r, d, LM), and lower values indicate a superior performance on the error metrics ($RMSE$, MAE). The RF and MLP models were similar in terms of both efficiency and error, while the MLR model performed the worst across all measures.

Table 3. Model performance metrics for Solomon Islands.

Model	r	d	LM	RMSE	MAE
MLR	0.9155	0.9068	0.6128	0.0886	0.0696
RF	0.9912	0.9911	0.8775	0.0296	0.022
MLP	0.9913	0.9911	0.8803	0.0294	0.0215
CNN-BiLSTM	0.9989	0.9987	0.9532	0.0113	0.0084

Table 4 shows the model performance metrics for the FSM, with the CNN-BiLSTM model once again achieving a superior performance across all metrics. The RF and MLP models were again similar in terms of both efficiency and error, while the MLR model performed the worst across all measures once more.

Table 4. Model performance metrics for FSM.

Model	r	d	LM	RMSE	MAE
MLR	0.9499	0.9355	0.654	0.1044	0.0821
RF	0.9507	0.9408	0.6816	0.0982	0.0756
MLP	0.9898	0.9885	0.8682	0.0425	0.0313
CNN-BiLSTM	0.9909	0.9891	0.8723	0.0415	0.0303

Scatterplots of the forecasted (MSL^{for}) versus observed (MSL^{obs}) mean sea levels for the two study sites using the four models provide a visual comparison. Each scatterplot shows the coefficient of determination (r^2) with the goodness of fit between the predicted and the observed MSL and a least-square fitting line with the corresponding equation:

$$y = mx + c \tag{12}$$

where y represents MSL^{for}, m is the gradient, x represents MSL^{obs} and c is the y-intercept.

Figures 7 and 8 show that the CNN-BiLSTM model displayed a significant performance with a higher r^2 value than the MLP, the RF model and especially the MLR model for both the Solomon Islands and FSM, though the forecasting using the CNN-BiLSTM model for the Solomons TG station performed slightly better than for the FSM station. The magnitudes registered using this model for both stations were the closest to unity, which in pairs $(m|r^2)$ are 0.988 | 0.9979 for the Solomon Islands, followed by 0.9856 | 0.9818 for the FSM.

The MLP model also performed well for both study sites, though particularly for the Solomon Islands. Additionally, the y-intercepts were found to be closer to the ideal value of zero for the MLP and CNN-BiLSTM models (0.0049 and 0.0012 for the Solomon Islands and the FSM, respectively, with the CNN-BiLSTM and 0.0044 and 0.0079 with the MLP).

Histograms are another effective graphical method of indicating the predictive performance of models, showing the frequency of prediction error (PE) and its distribution within the partitioned "bins". Figure 9 depicts histograms of the absolute PE of each model for both the Solomon Islands and FSM.

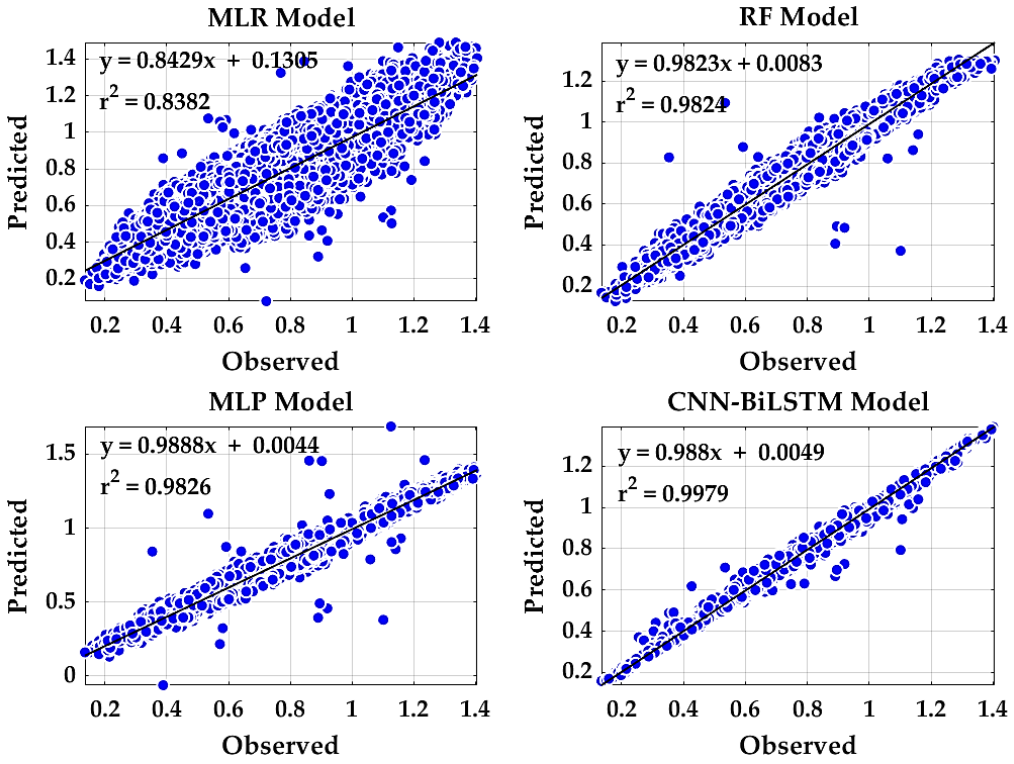

Figure 7. Scatter plots for Solomon Islands showing model accuracy in terms of r^2.

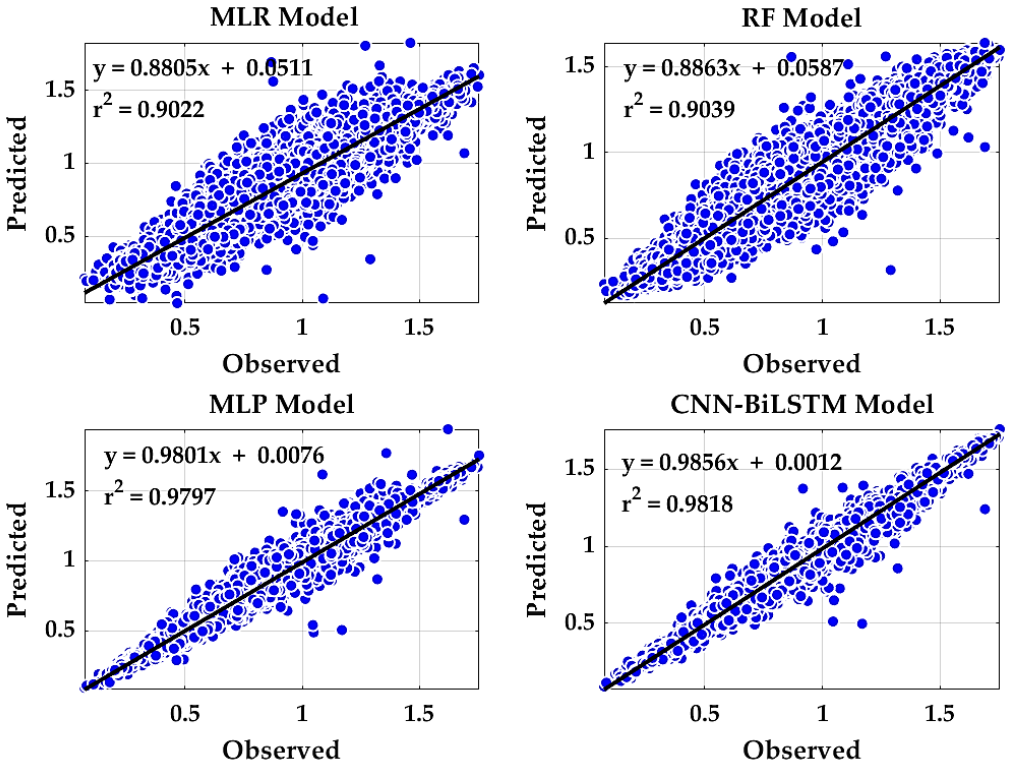

Figure 8. Scatter plots for FSM showing model accuracy in terms of r^2.

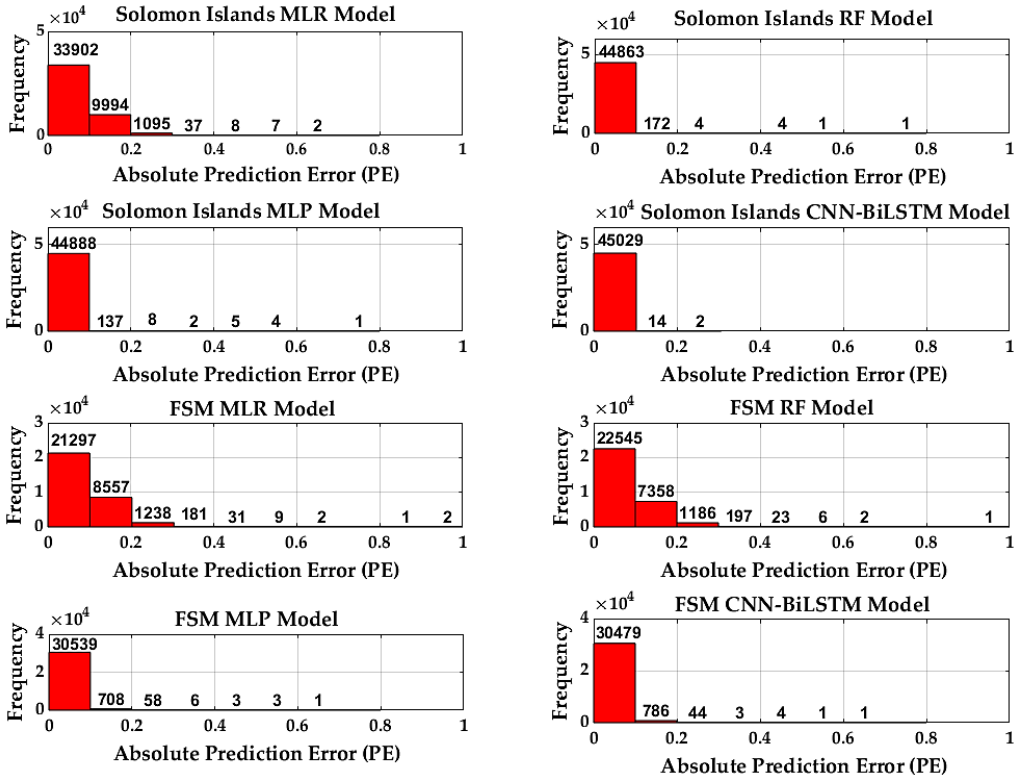

Figure 9. Histograms of absolute prediction errors for both islands according to AI model.

As can be seen in Figure 9, the CNN-BiLSTM model achieved a lower absolute prediction error than any other model for the Solomon Islands and performed comparably with the MLP model for the FSM. In addition, the CNN-BiLSTM model achieved the highest accuracy in terms of r^2 according to the scatterplots analysed in Figures 7 and 8, and outperformed the three other models examined according to all five efficiency and error metrics presented in Tables 3 and 4. The CNN-BiLSTM model thus represents the optimal model for predicting sea levels in the current comparison, and these predictions will be discussed in Section 4, following the presentation of the wetland classification results below.

3.2. Classification of Wetlands

To evaluate the use of RS and ML for the detection of coastal vegetation changes in the Solomon Islands and the FSM, areas likely to be wetlands were identified from satellite images, as described in Section 2. Figure 10 depicts the wetland extraction results for the FSM study location of Pohnpei, the largest island in the group, and the site of the Micronesian TG station. The satellite images for the study sites are obtained from the Landsat 7 and 8 Surface Reflectance Tier 1 collection. The images are at a resolution of 30 m. The Landsat data include a "pixel_qa" band, which can be used to create a function for masking clouds. Spectral indices are added for the wetland mapping, which includes the normalised difference vegetation index (NDVI), Normalised Difference Moisture Index (NDMI), Modified Normalised Difference Water Index (MNDWI) and green chlorophyll vegetation index (GCVI). The image is then reduced using the median function and geometry clipped to the area of interest. The bands of interest are selected, and samples are created for classification using the Random Forest model. Figures 10 and 11 show the extraction results.

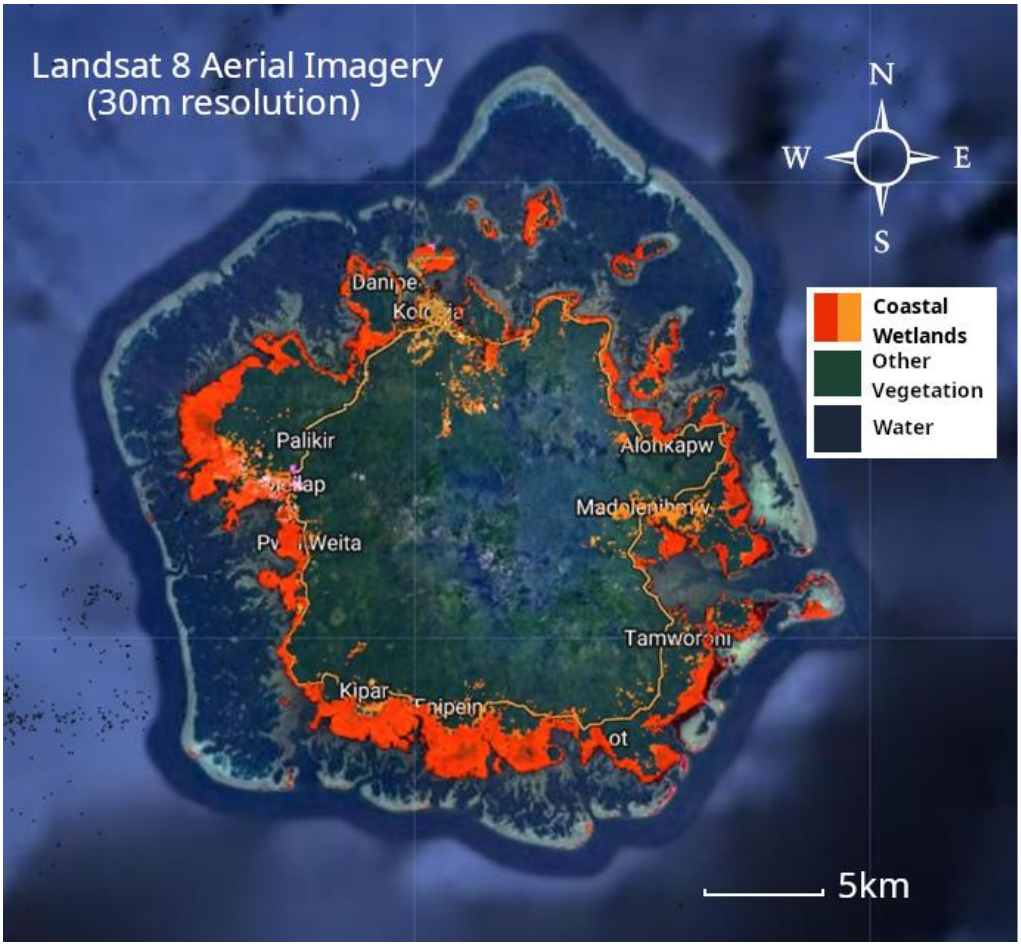

Figure 10. Coastal wetland vegetation extraction for FSM study location derived from Landsat Surface Reflectance Tier 1 imagery dataset.

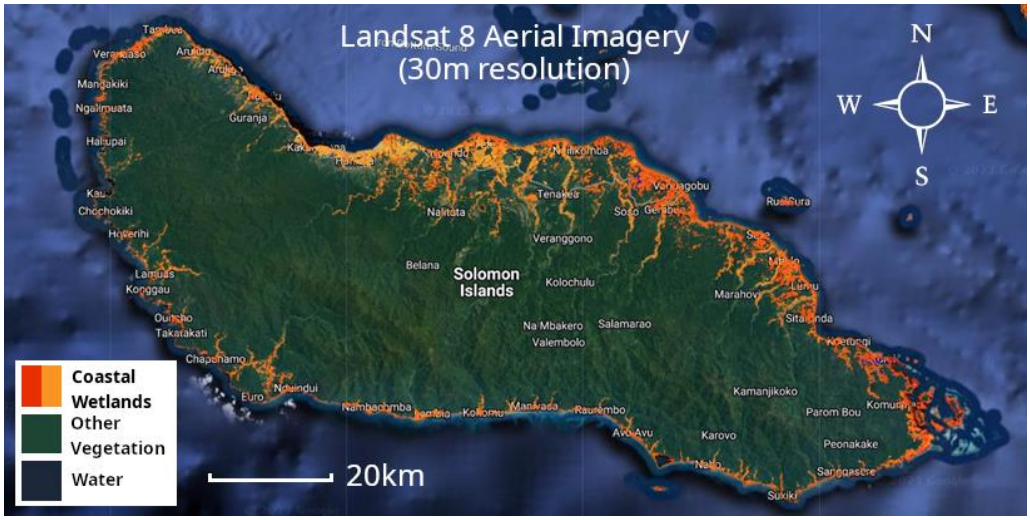

Figure 11. Coastal wetland vegetation extraction for Solomon Islands study location.

Figure 11 similarly depicts the wetland extraction for the Solomon Islands study location of Guadalcanal, the largest island in the group and the site of the TG station.

A comparison of the coastal wetland extent detected in each study area in 2009 and 2022 is shown in Table 5. A greater decline is seen for Guadalcanal in the Solomon Islands.

Table 5 shows the accuracy of these classifications, with the model achieving an accuracy of 0.98387 for the Solomon Islands and 0.99231 for the FSM.

Table 5. Wetland classification details using Random Forest model for Solomon Islands and FSM.

Study Area	Samples Taken	Training	Testing	Overall Accuracy	Percentage Accuracy	Kappa
Guadalcanal, SI	330	264	66	0.9834	98.34%	0.92
Pohnpei, FSM	340	272	68	0.9923	99.23%	0.94

According to the results presented in Table 5, the method employed proved highly accurate in identifying wetland areas on the island of Guadalcanal in the Solomons, and in particular, on Pohnpei in the FSM, with Kappa values of 0.92 and 0.94, respectively. The findings of this classification in relation to wetland change as outlined in the second research question will be discussed in Section 4 below, following the discussion of SLR.

4. Discussion

4.1. Prediction of Sea Level Trends

Based on the results presented in Section 3.1 above, Figure 12 shows the annual mean sea level trends for the Solomon Islands study site and the FSM study site, superimposed with the linear annual sea level mean (in red) and the optimal CNN-BiLSTM model (in orange). The annual rate of rise at the Solomon Islands study site of Honiara, Guadalcanal, was 0.0063 m/year (6.3 mm/year) between 1994 and 2022, and at the FSM study site of Pohnpei, it was 0.0072 m/year (7.2 mm/year) between 2001 and 2022. As can be seen from the orange lines in Figure 12, the CNN-BiLSTM model approximates the observed MSL, as outlined in Section 3.1, particularly for the Solomon Islands study site.

The rates of 6.3 and 7.2 mm/year may appear low in comparison with the ranges of 7–10 and up to 12 mm/year in Micronesia and the Solomon Islands quoted in the literature and media accounts. However, most of the existing research agrees that the long-term trends of SLR in the Solomons have averaged 7 mm/year, sometimes reaching 10–11 mm/year (±3 mm/year). Within this context, the results of the present study agree well with the observations of previous studies.

With the benefit of more than two decades of data, the present study demonstrates that the overall rate of rise at this location is less extreme than the 21.4 mm/year calculated during the early 2000s, based on less than five years' data. However, just because the SLR at Pohnpei is not three times higher than anywhere else in the PSLGM network does not imply that it is significant. The SLR near Honiara over the same period as that measured for Pohnpei in the FSM (2001–2022) was 6.0 mm/year, compared to Pohnpei's 7.2 mm/year. Overall, the rates of rise for both the FSM and Solomon Islands found in the present study are well above the average rate of global SLR, which, according to NASA satellite data (https://sealevel.nasa.gov/faq/8/is-the-rate-of-sea-level-rise-increasing/, accessed on 19 March 2023), has taken place at 3.4 mm/year since 1993.

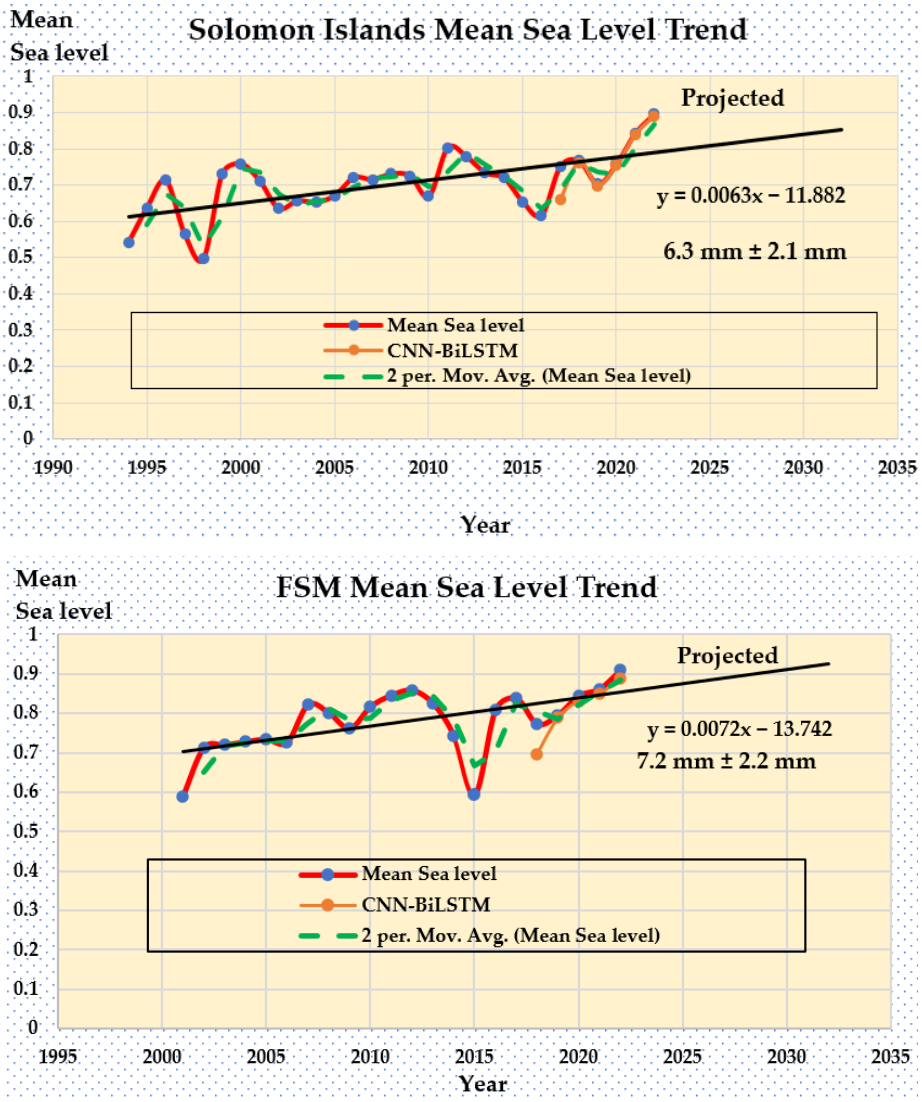

Figure 12. Annual MSL trend from 1994 to 2022 for the Solomon Islands study site Guadalcanal, and 2001 to 2022 for the FSM study site Pohnpei, with CNN-BiLSTM predicted mean and the linear annual MSL.

4.2. Detection of Wetland Change

The mean NDVI for the Solomon Islands study region of Guadalcanal and the FSM study region of Pohnpei is shown in Figure 13. Decreases in the NDVI indicate a decrease in biomass [41].

Figure 13 shows that overall, the mean NDVI in the FSM is higher than in the Solomon Islands, ranging between around 0.4 and 0.8, in comparison with a range of 0.3 to 0.7 in the Solomon Islands. This may indicate healthier and/or denser coverage in the FSM. However, there is a slight decrease for the trend in NDVI values in Pohnpei. Areas classified as wetland in the satellite images from 2009 and 2022, using the RF method evaluated in Section 3.2 above, were used to detect the changes in total wetland areas (in hectares) for both Guadalcanal and Pohnpei. The detected change in the coastal wetland areas over this period is displayed in Table 6 below. The area detected as wetlands declined over the past decade on both islands, with an apparent loss of 5599 ha on Guadalcanal in the Solomon Islands and 1410 ha on Pohnpei in the FSM.

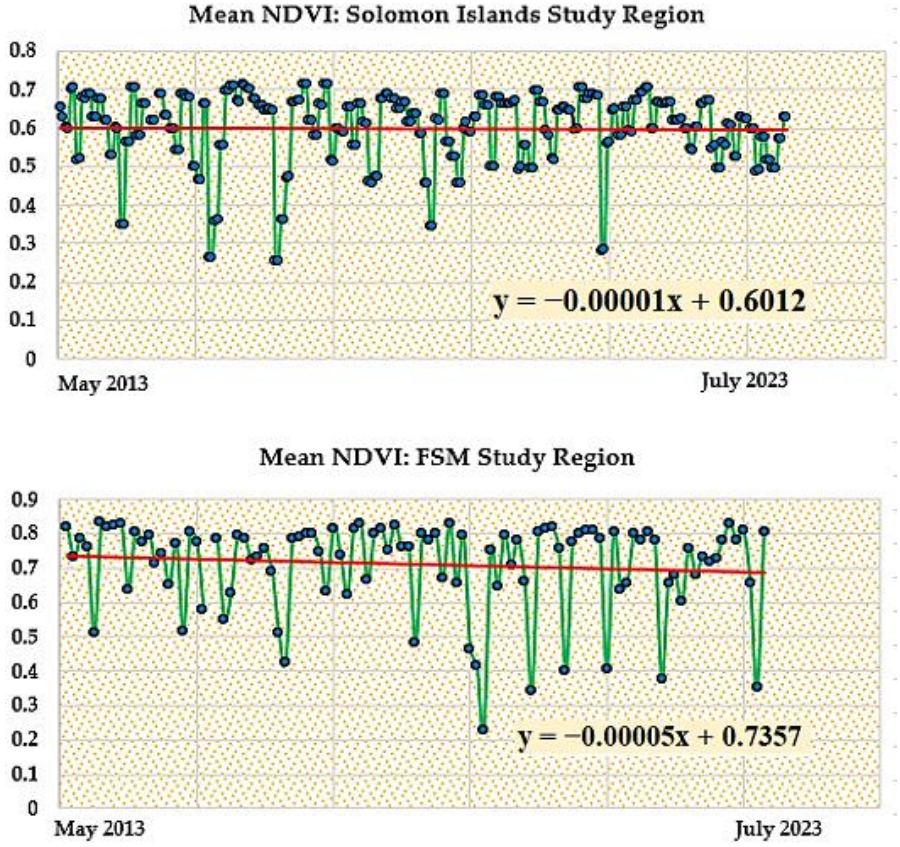

Figure 13. Wetland mean NDVI for Solomon Islands and FSM study location derived from Landsat Surface Reflectance Tier 1 imagery dataset.

Table 6. Wetland change detection from 2009 to 2022 for both study areas.

Study Area Wetland Classified Image	2009 Area	2022 Area	Detected Decline in Coastal Wetland Area from 2009 to 2022
Guadalcanal, SI	12,161.14 ha	6562.11 ha	5599.03 ha
Pohnpei, FSM	7371.14 ha	5960.59 ha	1410.55 ha

While the coastal wetland includes many types of vegetation, mangroves are an important feature and play a significant role in the coastal ecosystem. The darker orange patches in Figures 10 and 11 are more likely to be mangrove vegetation. The statistics obtained via the GMW dataset, presented in Appendix A, provide insight into the vitality of mangroves specifically at both the national and island levels. In the FSM, 9084 ha (or 90.84 km^2) of mangroves was detected using GMW in 1996, declining to 8794 ha (or 87.94 km^2) by 2020. In the Solomon Islands, 52,731 ha (or 527.31 km^2) of mangroves was detected using the 1996 satellite images, declining to 52,651 ha (or 526.51 km^2) in 2020. The area detected as mangrove habitat on Pohnpei, the FSM, was 5696 ha in 1996, declining to 5373 ha in 2020, representing a loss of 296 ha. The linear coverage of Pohnpei's coastline also showed a decline. In 1996, the GMW dataset indicates that 204.95 km of the island's coast was covered in mangroves, a linear coverage of 85.46%. By 2020, this figure had decreased to 202.51 km, or 84.44%. It is important to note, however, that none of these losses have been linear.

The FSM, and Pohnpei in particular, recorded decreases in its total mangrove habitat between 1996 and 2009, followed by a significant rise in 2010, and then a period of relative stability at approximately 1996 levels. The two most recent years of data available suggest that mangrove habitats may again be decreasing, almost reaching their lowest point on record once more. These findings may be compared to a recent study of Pohnpei by

Woltz et al. [47], which included a field survey. According to Woltz et al., Pohnpei had 6377 ha of mangrove in 1983, and the total gain over the 35 years to 2018 was 49 ha, the result of 16 ha lost, and a 65 ha gain in other locations. Mangroves cover all sides of Pohnpei's coasts but appear most concentrated on the leeward (west–southwest) side, which appears consistent with the areas detected as likely to be mangroves in the present study (as shown in Figures 10 and 11) using the Landsat images.

The mangrove habitats of Guadalcanal, the Solomon Islands, detected using GMW represented 1167 ha in 1996, while in 2020, only 1105 ha was detected, representing a loss of 62 ha. The linear coverage of Guadalcanal's coastline between 1996 and 2020 appears remarkably stable, ranging between 16.02% and 16.31%. The most recent estimates of mangrove habitats for both the FSM and Solomon Islands identified in the literature were produced by Jia et al. [48], who made use of 10 m resolution imagery from Sentinel-2. Significantly, their estimates are also the most different from any previous study. While the paper does not provide individual country breakdowns, these figures were obtained from the supplementary data, wherein it is stated that the total mangrove area for the FSM was 56.54 km^2 and 332.68 km^2 for the Solomon Islands. Both figures are substantially lower than the 87.94 km^2 and 526.51 km^2 areas identified to be mangroves in the FSM and Solomon Islands using the GMW data in the present study. Given that higher-resolution images should prove helpful in detecting smaller mangrove patches, the lower area detected by Jia et al. may appear surprising. However, the authors note that GMW v3.0 uses GMW v2.5 as a baseline, detecting changes using L-band SAR, which has difficulty discerning mangrove forests from other woody wetlands. Accordingly, Jia et al. speculate that some of the lowland wet forests adjacent to the mangrove swamps may be misclassified as mangroves in the GMW data, highlighting the need for validation via field survey data.

5. Conclusions

This study utilised data-driven AI models to predict the sea level using a range of climate input variables. It successfully used TG data to predict the sea level in the Solomon Islands and FSM from 1994 to 2022. The geodetic variables of water, air temperature, barometric pressure, wind direction, gust and speed were used to train the AI models. The hybrid CNN-BiLSTM model provided the most accurate sea level prediction for both study sites. The mean sea level was used to provide an annual trend analysis, which revealed a projected increase for both locations above the global trends. The mean sea levels were found to have risen 6.0 mm/year over the last two decades in the Solomon Islands (a slight decrease compared to the 6.3 ± 2.1 mm/year rate of rise since 1994) and 7.2 ± 2.2 mm/year in the FSM. The SLR in both locations appears significantly higher than the global averages.

The identification of wetlands in general in small island nations such as the FSM and Solomon Islands can be difficult, with challenges including the availability of cloud-free scenes and the detection of small, yet ecologically significant, patches of vegetation. The detection of coastal vegetation changes was carried out using data from Landsat satellite images and an RF model to examine the coastal wetlands on Guadalcanal and Pohnpei and data from GMW to examine mangrove trends in the Solomon Islands and FSM more broadly. A high level of accuracy (>0.98) was achieved using the RF model at both study sites. The coastal wetlands in general were found to have decreased in extent. Analysis of vegetation health is of particular importance in the Solomon Islands given the detrimental effects of logging observed by Minter and van der Ploeg [49]. The mean NDVI in the Pohnpei region in the FSM (ranging between 0.4 and 0.8) was found to be higher than in the Guadalcanal region in the Solomon Islands (ranging between 0.3 and 0.7), consistent with the other results of the present study. Apparent losses in wetlands were recorded in both study areas using the Landsat satellite imagery analysis, while such decreases may be associated with logging and other climate change effects, including a rising sea level.

The findings of the present study demonstrate the importance of long-term monitoring and the importance of taking the length of records into account. Shorter records are more susceptible to extremes and may mask the true effects of SLR. As PSGLM records

continue to lengthen, future research will be able to make more accurate observations (and hence, predictions) of the MSL. While the wetland detection using satellite imagery and RF classification utilised in the present study achieved high levels of accuracy, comparable with or exceeding previous studies, more research is required in this area, including fieldwork, which can provide ground truth data.

Author Contributions: Conceptualisation, N.R. and S.P.-N.; methodology, N.R.; software, N.R.; validation, N.R. and S.P.-N.; formal analysis, N.R.; investigation, N.R. and S.P.-N.; resources, N.R. and S.P.-N.; data curation, N.R. and S.P.-N.; writing—original draft preparation, N.R. and S.P.-N.; writing—review and editing, N.R. and S.P.-N.; visualisation, N.R. and S.P.-N.; supervision, N.R.; project administration, N.R. All authors have read and agreed to the published version of the manuscript.

Funding: This research received no external funding.

Data Availability Statement: Data are contained within the article.

Conflicts of Interest: The authors declare no conflicts of interest.

Appendix A

Table A1. Annual mean sea level (MSL), calculated from PSLGM data, and mangrove area and coverage in the Solomon Islands and Federated States of Micronesia, sourced from GMW.

	Solomon Islands			Federated States of Micronesia		
	Annual MSL (m above TG Zero)	**Total (Guadalcanal) Mangrove Area (km^2)**	**National (Guadalcanal) Coastline Coverage (km)**	**Annual MSL (m above TG Zero)**	**Total (Pohnpei) Mangrove Area (km^2)**	**National (Pohnpei) Coastline Coverage (km)**
1994	0.5403					
1995	0.6377					
1996	0.7129	527.31 (11.67)	4371.56 (84.44)		90.84 (56.69)	402.71 (204.95)
1997	0.5650					
1998	0.4962					
1999	0.7309					
2000	0.7589					
2001	0.7112			0.5900		
2002	0.6356			0.7131		
2003	0.6563			0.7199		
2004	0.6528			0.7279		
2005	0.6710			0.7345		
2006	0.7204			0.7266		
2007	0.7151	529.25 (11.63)	4359.06 (84.25)	0.8220	88.18 (54.61)	399.6 (203.11)
2008	0.7307	530.04 (11.62)	4357.74 (84.95)	0.8012	88.01 (54.61)	399.05 (203.11)
2009	0.7253	530.84 (11.71)	4352.74 (84.91)	0.7616	87.91 (54.51)	397.65 (202.36)
2010	0.6684	528.98 (11.77)	4348.12 (84.82)	0.8169	90.17 (56.56)	400.91 (204.86)
2011	0.8024			0.8455		
2012	0.7783			0.8585		
2013	0.7337			0.8251		

Table A1. *Cont.*

	Solomon Islands			Federated States of Micronesia		
	Annual MSL (m above TG Zero)	**Total (Guadalcanal) Mangrove Area (km^2)**	**National (Guadalcanal) Coastline Coverage (km)**	**Annual MSL (m above TG Zero)**	**Total (Pohnpei) Mangrove Area (km^2)**	**National (Pohnpei) Coastline Coverage (km)**
2014	0.7191			0.7431		
2015	0.6536	525.48	4339.18 (84.85)	0.5936	90.69	402.17 (204.86)
2016	0.6164	523.58	4337.32 (84.91)	0.8090	90.69	402.17 (204.86)
2017	0.7517	522.21	4330.31 (84.91)	0.8387	90.69	402.17 (204.86)
2018	0.7663	524.71	4332 (84.88)	0.7727	90.69	402.17 (204.86)
2019	0.7022	527.5	4343.49 (84.25)	0.7961	88.18	398.59 (202.39)
2020	0.7582	526.51	4346.61 (83.44)	0.8447	87.94	398.49 (202.51)
2021	0.8429			0.8619		
2022	0.8950			0.9093		

References

1. Monnereau, I.; Abraham, S. Limits to Autonomous Adaptation in Response to Coastal Erosion in Kosrae, Micronesia. *Int. J. Glob. Warm.* **2013**, *5*, 416–432. [CrossRef]
2. Ha'apio, M.O.; Morrison, K.; Gonzalez, R.; Wairiu, M.; Holland, E. Limits and Barriers to Transformation: A Case Study of April Ridge Relocation Initiative, East Honiara, Solomon Islands. In *Climate Change Impacts and Adaptation Strategies for Coastal Communities*; Climate Change Management Book Series; Springer: Berlin/Heidelberg, Germany, 2018; pp. 455–470. [CrossRef]
3. Boero, F.; Treguier, A.M.; Philippart, C.; Huse, G.; Gault, J.; Schneider, R.; Cummins, V.; Garcia-Soto, C.; Patterson, D.; Lacroix, D.; et al. Navigating the Future V: Marine Science for a Sustainable Future. *Zenodo* **2019**. [CrossRef]
4. Timmermann, A.; McGregor, S.; Jin, F.-F. Wind Effects on Past and Future Regional Sea Level Trends in the Southern Indo-Pacific. *J. Clim.* **2010**, *23*, 4429–4437. [CrossRef]
5. Isiaka, I.; Ndukwe, K.; Chibuike, U. Mean Sea Level: The Effect of the Rise in the Environment. *J. Geoinform. Environ. Res.* **2021**, *2*, 92–102. [CrossRef]
6. Albert, S.; Bronen, R.; Tooler, N.; Leon, J.; Yee, D.; Ash, J.; Boseto, D.; Grinham, A. Heading for the Hills: Climate-Driven Community Relocations in the Solomon Islands and Alaska Provide Insight for a 1.5 °C Future. *Reg. Environ. Change* **2018**, *18*, 2261–2272. [CrossRef]
7. IPCC. *Climate Change 2022: Impacts, Adaptation and Vulnerability*; Cambridge University Press: Cambridge, UK, 2022. [CrossRef]
8. Church, J.A.; White, N.J.; Hunter, J.R. Sea-Level Rise at Tropical Pacific and Indian Ocean Islands. *Glob. Planet. Change* **2006**, *53*, 155–168. [CrossRef]
9. Klein, A. Eight Low-Lying Pacific Islands Swallowed Whole by Rising Seas. Available online: https://www.newscientist.com/article/2146594-eight-low-lying-pacific-islands-swallowed-whole-by-rising-seas/ (accessed on 16 March 2023).
10. Mcleod, E.; Hinkel, J.; Vafeidis, A.T.; Nicholls, R.J.; Harvey, N.; Salm, R. Sea-Level Rise Vulnerability in the Countries of the Coral Triangle. *Sustain. Sci.* **2010**, *5*, 207–222. [CrossRef]
11. André, L.V.; Van Wynsberge, S.; Chinain, M.; Andréfouët, S. An Appraisal of Systematic Conservation Planning for Pacific Ocean Tropical Islands Coastal Environments. *Mar. Pollut. Bull.* **2021**, *165*, 1121131. [CrossRef] [PubMed]
12. Gilman, E.; Van Lavieren, H.; Ellison, J.; Jungblut, V.; Wilson, L.; Areki, F.; Brighouse, G.; Bungitak, J.; Dus, E.; Kilman, M.; et al. *Pacific Island Mangroves in a Changing Climate and Rising Sea*; Regional Seas; United Nations Environment Programme: Nairobi, Kenya, 2006; ISBN 978-92-807-2741-8.
13. Raj, N.; Gharineiat, Z.; Ahmed, A.A.M.; Stepanyants, Y. Assessment and Prediction of Sea Level Trend in the South Pacific Region. *Remote Sens.* **2022**, *14*, 986. [CrossRef]
14. Tiggeloven, T.; Couasnon, A.; van Straaten, C.; Muis, S.; Ward, P.J. Exploring Deep Learning Capabilities for Surge Predictions in Coastal Areas. *Sci. Rep.* **2021**, *11*, 17224. [CrossRef] [PubMed]
15. Raj, N. Prediction of Sea Level with Vertical Land Movement Correction Using Deep Learning. *Mathematics* **2022**, *10*, 4533. [CrossRef]
16. Raj, N.; Brown, J. An EEMD-BiLSTM Algorithm Integrated with Boruta Random Forest Optimiser for Significant Wave Height Forecasting along Coastal Areas of Queensland, Australia. *Remote Sens.* **2021**, *13*, 1456. [CrossRef]
17. Moishin, M.; Deo, R.C.; Prasad, R.; Raj, N.; Abdulla, S. Designing Deep-Based Learning Flood Forecast Model with ConvLSTM Hybrid Algorithm. *IEEE Access* **2021**, *9*, 50982–50993. [CrossRef]

18. Sharma, E.; Deo, R.C.; Prasad, R.; Parisi, A.V.; Raj, N. Deep Air Quality Forecasts: Suspended Particulate Matter Modeling with Convolutional Neural and Long Short-Term Memory Networks. *IEEE Access* **2020**, *8*, 209503–209516. [CrossRef]
19. Berryman, A.; Turchin, P. Identifying the Density—Dependent Structure Underlying Ecological Time Series. *Oikos* **2001**, *92*, 265–270. [CrossRef]
20. Nkoro, E.; Uko, A.K. Autoregressive Distributed Lag (ARDL) Cointegration Technique: Application and Interpretation. *J. Stat. Econom. Methods* **2016**, *5*, 63–91.
21. Gaur, A.; Pachori, R.B.; Wang, H.; Prasad, G. An Automatic Subject Specific Intrinsic Mode Function Selection for Enhancing Two-Class EEG-Based Motor Imagery-Brain Computer Interface. *IEEE Sens.* **2019**, *19*, 6938–6947. [CrossRef]
22. Ur Rehman, N.; Aftab, H. Multivariate Variational Mode Decomposition. *IEEE Trans. Signal Process.* **2019**, *67*, 6039–6052. [CrossRef]
23. Alasadi, S.A.; Bhaya, W.S. Review of Data Preprocessing Techniques in Data Mining. *J. Eng. Appl. Sci.* **2017**, *12*, 4102–4107.
24. Lou, R.; Lv, Z.; Dang, S.; Su, T.; Li, X. Application of Machine Learning in Ocean Data. In *Multimedia Systems*; Springer: Berlin/Heidelberg, Germany, 2021. [CrossRef]
25. Atmaja, T.; Fukushi, K. Empowering Geo-Based AI Algorithm to Aid Coastal Flood Risk Analysis: A Review and Development Framework. *ISPRS Ann. Photogramm. Remote Sens. Spatial Inf. Sci.* **2022**, *V-3-2022*, 517–523. [CrossRef]
26. Rehman, S.; Sahana, M.; Hong, H.; Sajjad, H.; Ahmed, B.B. A Systematic Review on Approaches and Methods Used for Flood Vulnerability Assessment: Framework for Future Research. *Nat. Hazards* **2019**, *96*, 975–998. [CrossRef]
27. Breiman, L. Random Forests. *Mach. Learn.* **2001**, *45*, 5–32. [CrossRef]
28. Tahraoui, H.; Amrane, A.; Belhadj, A.-E.; Zhang, J. Modeling the Organic Matter of Water Using the Decision Tree Coupled with Bootstrap Aggregated and Least-Squares Boosting. *Environ. Technol. Innov.* **2022**, *27*, 102419. [CrossRef]
29. Ahmed, A.; Deo, R.C.; Feng, Q.; Ghahramani, A.; Raj, N.; Yin, Z.; Yang, L. Hybrid Deep Learning Method for a Week-Ahead Evapotranspiration Forecasting. *Stoch. Environ. Res. Risk Assess.* **2022**, *36*, 831–849. [CrossRef]
30. Hopp, D. Using Machine Learning to Make Government Spending Greener. *Stat. J. IAOS* **2022**, *38*, 1053–1065. [CrossRef]
31. Latif, S.D.; Chong, K.L.; Ahmed, A.N.; Huang, Y.F.; Sherif, M.; El-Shafie, A. Sediment Load Prediction in Johor River: Deep Learning versus Machine Learning Models. *Appl. Water Sci.* **2023**, *13*, 79. [CrossRef]
32. Bagheri, M.; Ibrahim, Z.Z.; Wolf, I.D.; Akhir, M.F.; Talaat, W.I.A.W.; Oryani, B. Sea-Level Projections Using a NARX-NN Model of Tide Gauge Data for the Coastal City of Kuala Terengganu in Malaysia. *Environ. Sci. Pollut. Res.* **2022**, *30*, 81839–81857. [CrossRef]
33. Ahmed, A.; Deo, R.C.; Feng, Q.; Ghahramani, A.; Raj, N.; Yin, Z.; Yang, L. Deep Learning Hybrid Model with Boruta-Random Forest Optimiser Algorithm for Streamflow Forecasting with Climate Mode Indices, Rainfall, and Periodicity. *J. Hydrol.* **2021**, *599*, 126350. [CrossRef]
34. Tran, T.T.; Pham, N.H.; Pham, Q.B.; Pham, T.L.; Ngo, X.Q.; Nguyen, D.L.; Nguyen, P.N.; Veettil, B.K. Performances of Different Machine Learning Algorithms for Predicting Saltwater Intrusion in the Vietnamese Mekong Delta Using Limited Input Data: A Study from Ham Luong River. *Water Resour.* **2022**, *49*, 391–401. [CrossRef]
35. Hodson, T.O. Root-Mean-Square Error (RMSE) or Mean Absolute Error (MAE): When to Use Them or Not. *Geosci. Model Dev.* **2022**, *15*, 5481–5487. [CrossRef]
36. Willmott, C.J.; Matsumura, K. Advantages of the Mean Absolute Error (MAE) Over the Root Mean Square Error (RMSE) in Assessing Average Model Performance. *Clim. Res.* **2005**, *30*, 79–82. [CrossRef]
37. Shi, T.; Liu, J.; Hu, Z.; Wang, J.; Wu, G. New Spectral Metrics for Mangrove Forest Identification. *Remote Sens. Lett.* **2016**, *7*, 885–894. [CrossRef]
38. Xu, H. Modification of Normalised Difference Water Index (NDWI) to Enhance Open Water Features in Remotely Sensed Imagery. *Int. J. Remote Sens.* **2006**, *27*, 3025–3033. [CrossRef]
39. Melillos, G.; Hadjimitsis, D.G. Using Simple Ratio (SR) Vegetation Index to Detect Deep Man-Made Infrastructures in Cyprus. In *Detection and Sensing of Mines, Explosive Objects, and Obscured Targets XXV*; SPIE: Bellingham, WA, USA, 2020. [CrossRef]
40. Jubeh, G.; Mimi, Z. Governance and Climate Vulnerability Index. *Water Resour. Manag.* **2012**, *26*, 4147–4162. [CrossRef]
41. Islam, M.S.; Uddin, M.A.; Hossain, M.A. Assessing the Dynamics of Land Cover and Shoreline Changes of Nijhum Dwip (Island) of Bangladesh Using Remote Sensing and GIS Techniques. *Reg. Stud. Mar. Sci.* **2021**, *41*, 101578. [CrossRef]
42. Samanta, S.; Hazra, S.; Mondal, P.P.; Chanda, A.; Giri, S.; French, J.R.; Nicholls, R.J. Assessment and Attribution of Mangrove Forest Changes in the Indian Sundarbans from 2000 to 2020. *Remote Sens.* **2021**, *13*, 4957. [CrossRef]
43. Xiao, H.; Su, F.; Fu, D.; Wang, Q.; Huang, C. Coastal Mangrove Response to Marine Erosion: Evaluating the Impacts of Spatial Distribution and Vegetation Growth in Bangkok Bay from 1987 to 2017. *Remote Sens.* **2020**, *12*, 220. [CrossRef]
44. da Costa Cavalcante, J.; de Lima, A.M.M.; da Silva, J.C.C.; de Holanda, B.S.; Almeida, C.A. Temporal Analysis of the Mangrove Forest at the Mocajuba River Hydrographic Basin-Pará. *Floresta Ambient.* **2021**, *28*, e20200073. [CrossRef]
45. Mohanty, P.C.; Shetty, S.; Mahendra, R.S.; Nayak, R.K.; Sharma, L.K.; Rama Rao, E.P. Spatio-Temporal Changes of Mangrove Cover and Its Impact on Bio-Carbon Flux along the West Bengal Coast, Northeast Coast of India. *Eur. J. Remote Sens.* **2021**, *54*, 525–537. [CrossRef]
46. Khedher, K.M.; Abu-Taweel, G.M.; Al-Fifi, Z.; Qoradi, M.D.; Al-khafaji, Z.; Halder, B.; Bandyopadhyay, J.; Shahid, S.; Essaied, L.; Yaseen, Z.M. Farasan Island of Saudi Arabia Confronts the Measurable Impacts of Global Warming in 45 Years. *Sci. Rep.* **2022**, *12*, 14322. [CrossRef] [PubMed]

47. Woltz, V.L.; Peneva-Reed, E.I.; Zhu, Z.; Bullock, E.L.; MacKenzie, R.A.; Apwong, M.; Krauss, K.W.; Gesch, D.B. A Comprehensive Assessment of Mangrove Species and Carbon Stock on Pohnpei, Micronesia. *PLoS ONE* **2022**, *17*, e0271589. [CrossRef] [PubMed]
48. Jia, M.; Wang, Z.; Mao, D.; Ren, C.; Song, K.; Zhao, C.; Wang, C.; Xiao, X.; Wang, Y. Mapping Global Distribution of Mangrove Forests at 10-m Resolution. *Sci. Bull.* **2023**, *68*, 1306–1316. [CrossRef] [PubMed]
49. Minter, T.; Van Der Ploeg, J. "Our Happy Hour Became a Hungry Hour": Logging, Subsistence and Social Relations in Solomon Islands. *Int. Forest. Rev.* **2023**, *25*, 113–135. [CrossRef]